NIST Technical Note
NIST TN 2344

Measuring the effectiveness of Linnik blind deconvolution in nanoscale electron microscopy, by computing image Lipschitz exponents

Alfred S. Carasso
Andras E. Vladar

This publication is available free of charge from:
https://doi.org/10.6028/NIST.TN.2344

NATIONAL INSTITUTE OF STANDARDS AND TECHNOLOGY
U.S. DEPARTMENT OF COMMERCE

NIST Technical Note
NIST TN 2344

Measuring the effectiveness of Linnik blind deconvolution in nanoscale electron microscopy, by computing image Lipschitz exponents

Alfred S. Carasso [1], Andras E. Vladar [2]

[1] Applied and Computational Mathematics Division, Information Technology Laboratory, NIST, Gaithersburg, Maryland, USA

[2] Microsystems and Nanotechnology Division, Physical Measurement Laboratory, NIST, Gaithersburg, Maryland, USA

This publication is available free of charge from:
https://doi.org/10.6028/NIST.TN.2344

August 2025

U.S. Department of Commerce
Howard Lutnick, Secretary

National Institute of Standards and Technology
Craig Burkhardt, Acting Under Secretary of Commerce for Standards and Technology and Acting NIST Director

NIST Technical Series Publications: https://www.nist.gov/nist-research-library/nist-publications

Publication History

Approved by the NIST Editorial Review Board on 2025-07-25.

Suggested Citation

Alfred S. Carasso, Andras E. Vladar (2025). Measuring the effectiveness of Linnik blind deconvolution in nanoscale electron microscopy, by computing image Lipschitz exponents. (National Institute of Standards and Technology, Gaithersburg, MD) NIST Technical Note (TN) 2344. DOI:10.6028/NIST.TN.2344

Author Names and ORCID Identifiers

Alfred S. Carasso (0000-0002-4182-0991); Andras E. Vladar (0000-0002-8823-6098).

Abstract

A large class of images $f(x, y)$, including nanoscale electron microscopy images, are not of bounded variation, but belong to Lipschitz (Besov) spaces $\Lambda(\alpha, 1, \infty)$. The parameter α, where $0 < \alpha < 1$, is called the Lipschitz exponent of $f(x, y)$, and it measures the natural *unsmoothness* of $f(x, y)$, provided that image is largely *noise free*. The present paper computes the Lipschitz exponents achieved in a previous paper, [1], where several electron microscopy images were deblurred using Linnik blind deconvolution. The present computations show that the Lipschitz exponents in these microscopy images were reduced by more than 33% typically, reflecting the recovery of the valuable small scale information that was realized in [1].

Keywords

SEM images; HIM images; image sharpening; blind deconvolution; Linnik point spread functions; time-reversed logarithmic diffusion equations; Besov spaces; Lipschitz exponents.

Table of Contents

List of Figures

1. Introduction

The present paper is a sequel to [1], where Linnik point spread functions were successfully applied in blind deconvolution of four scanning electron microscope (SEM) images, and four Helium ion microscope (HIM) images. Using ideas previously developed in [2], [3], [4], and [5], we now compute and highlight the improved *Lipschitz exponents* that result from the successful image deblurring presented in [1]. As noted in [2], most natural images are not of bounded variation. However, a large class of images $f(x_1, x_2)$, including nanoscale electron microscopy images, belong to Lipschitz (Besov) spaces $\Lambda(\alpha, 1, \infty)$ of functions with finite seminorm $\| f \|_{\alpha,1,\infty}$. Here, with $x = (x_1, x_2),\ h = (h_1, h_2), \in R^2$, and fixed α with $0 < \alpha < 1$, the seminorm $\| f \|_{\alpha,1,\infty} \equiv Sup_{h \in R^2}\{|h|^{-\alpha} \| f(x+h) - f(x) \|_1\}$. The parameter α is called the Lipschitz exponent of $f(x)$, and it measures the natural unsmoothness of the image, provided that image is relatively *noise free*. Sharp astronomical images, such as are shown in [3] and [4], typically have low Lipschitz exponents. Functions with larger α are "smoother" than functions with smaller α, and if $0 < \alpha_1 < \alpha_2,\ \Lambda(\alpha_2, 1, \infty) \subset \Lambda(\alpha_1, 1, \infty)$. Functions of bounded variation have $\alpha = 1.0$.

2. The Lipschitz (Besov) space and the Poisson singular integral

Define the Fourier transform $\hat{h}(\xi, \eta)$ of $h(x, y) \in L^1(R^2)$ by

$$F\{h\} = \hat{h}(\xi, \eta) \equiv \int_{R^2} h(x, y) e^{-2\pi i(\xi x + \eta y)} dx dy. \tag{1}$$

For fixed $t > 0$, consider the Poisson kernel in R^2

$$\psi(x, y, t) = \frac{t}{2\pi(x^2 + y^2 + t^2)^{3/2}}, \qquad (x, y) \in R^2. \tag{2}$$

We have

$$\hat{\psi}(\xi, \eta, t) = e^{-t\rho}, \qquad \rho = \sqrt{\xi^2 + \eta^2}. \tag{3}$$

For each $t > 0$, consider the linear operator U^t on $L^1(R^2)$ given by

$$U^t f = \int_{R^2} \psi(u, v, t) f(x - u, y - v) du dv. \tag{4}$$

With U^0 the identity operator, we have that for $s, t \geq 0,\ U^t U^s = U^{t+s}$. In fact, $\{U^t\}_{t\geq 0}$ is a holomorphic semigroup on $L^1(R^2)$. The following result is proved in [6].

Theorem 1 *Let $U^t,\ t > 0$, be the above Poisson operator, and let $0 < \alpha < 1$. Then, $f \in \Lambda(\alpha, 1, \infty)$ if and only if*

$$\sup_{t>0}\ t^{-\alpha} \parallel U^t f - f \parallel_1 <\ \infty. \tag{5}$$

In [2], the above theorem is used as the basis for computing a value of α associated with a given f in $L^1(R^2)$. A discretized version of $\{\parallel U^t f - f \parallel_1 / \parallel f \parallel_1\}$, is considered, and sequences $\mu_n = \{\parallel U^{t_n} f - f \parallel_1 / \parallel f \parallel_1\}$, with $t_n \downarrow 0$, are studied. The aim is to locate an appropriate curve $\mu(t) = Ct^\alpha,\ 0 < t \leq \bar{t}$, with $C > 0,\ 0 < \alpha < 1$, that can majorize any such sequence (t_n, μ_n). This would imply $\parallel U^t f - f \parallel_1 \leq C \parallel f \parallel_1 t^\alpha,\ 0 < t \leq \bar{t}$, and $f \in \Lambda(\alpha, 1, \infty)$.

2.1. Periodized problems

In Section 4 of [2], such a procedure is applied to an image $f(x, y)$ defined on the unit square Ω in R^2, from which it is extended by periodicity to all of R^2. Let

$$\hat{f}(\xi, \eta) = \int_\Omega f(x, y) e^{-2\pi i(\xi x + \eta y)} dx dy. \tag{6}$$

With $\psi(x, y, t)$ as in (2), define the periodized Poisson kernel $\psi^*(x, y, t)$ by

$$\psi^*(x, y, t) = \sum_{k,m=-\infty}^{\infty} \psi(x + k, y + m, t), \qquad t > 0,\ \ (x, y) \in R^2, \tag{7}$$

and let

$$U^t f = \int_\Omega \psi^*(u, v, t) f(x - u, y - v) du dv, \qquad t > 0. \tag{8}$$

The Poisson summation formula can be used to show that the periodized Poisson kernel has a complex Fourier series with Fourier coefficients again given by (3), but where ξ, η are now *integers* running from $-\infty$ to $+\infty$. Moreover,

$$(U^t f)(x, y) = \sum_{\xi,\eta=-\infty}^{\infty} e^{-t\rho} \hat{f}(\xi, \eta) e^{2\pi i(x\xi + y\eta)}, \qquad t > 0,\ \ \rho = \sqrt{\xi^2 + \eta^2}. \tag{9}$$

The factor $e^{-t\rho}$ assures uniform convergence of the Fourier series in (9). Let

$$(U^t f_N)(x,y) = \sum_{\xi,\eta=-N}^{N} e^{-t\rho} \hat{f}(\xi,\eta) e^{2\pi i(x\xi+y\eta)}, \qquad t>0, \quad \rho = \sqrt{\xi^2+\eta^2}. \tag{10}$$

With $(U^t f)(x,y)$ as in (9), $\| U^t f - U^t f_N \|_1$ can be made arbitrarily small by choosing N large enough in (10).

In application to $2J \times 2J$ digitized images $f(x,y)$, with $J > N$, the discrete Fourier transform, based on FFT algorithms, is used to form the Fourier coefficients $\hat{f}(\xi,\eta), \ -J \leq \xi, \eta \leq J$, followed by multiplication by $(e^{-t\rho} - 1)$. An inverse FFT yields an accurate approximation to $U^t f - f$ at each of the $2J \times 2J$ pixels. Using discrete L^1 norms, one can then create the discrete approximations

$$\mu_n = \| U^{t_n} f - f \|_1 \, / \, \| f \|_1, \qquad t_n > 0, \tag{11}$$

at successively smaller values of $t > 0$. Finding the value of the Lipschitz exponent α in a given image, requires plotting $\log \mu(t)$ versus $\log t$ as $t \downarrow 0$, and locating an appropriate majorizing straight line, using least squares fits. In Sections 4 and 5 of each of [2] and [3], the necessity of excluding very small values of t in such fits, is emphasized.

3. Applications to SEM and HIM electron microscopy

In [1], the results of Linnik blind deconvolution are displayed in that publication's Figures 5 through 12. In each of these 8 Figures in [1], the top row left image is the original microscopy image, while the top row right image is the Linnik deblurred image. In the bottom rows in each of these 8 Figures, the original and deblurred Fourier spectra are shown.

However, a key component of the results in [1], lies in the *preconditioning* that was applied to each of the 8 microscopy images, prior to Linnik deblurring. Each image was subjected to *adaptive histogram equalization* (AHE), which revealed useful information, while significantly magnifying noise. Following AHE, convolution with a low exponent Lévy stable density was applied to to each image, which greatly reduced that noise. These two steps define the precondioning that was applied in [1], prior to deconvolution.

In the present paper, these 8 Figures are displayed differently. The top left images are the *preconditioned*, rather than the original images, while the top right images are the Linnik deblurred images as before. In the bottom rows of each Figure, the Fourier spectra are replaced by the distinctive curved plots of $\log \mu(t)$ versus $\log t$, obtained by using Eqs. (11). A majorizing straight line, using least squares fits, accompanies each curve, as prescribed in

[2] and [3]. The resulting values for $C > 0,\ 0 < \alpha < 1$, are the parameters of the majorizing straight line in each of the bottom Figures. These values are listed in Table 1 below.

Table 1. Comparisons of Lipschitz exponent values before and after Linnik deblurring.

Figure	*Left* (C, α)	*Right* (C, α)	$\%\ \alpha$ *decrease*
$Figure\ 1\ (SEM)$	$C = 0.267,\ \alpha = 0.742$	$C = 0.412,\ \alpha = 0.570$	23%
$Figure\ 2\ (SEM)$	$C = 0.453,\ \alpha = 0.970$	$C = 0.170,\ \alpha = 0.646$	33%
$Figure\ 3\ (SEM)$	$C = 0.414,\ \alpha = 0.868$	$C = 0.734,\ \alpha = 0.581$	33%
$Figure\ 4\ (SEM)$	$C = 0.229,\ \alpha = 0.747$	$C = 0.516,\ \alpha = 0.503$	33%
$Figure\ 5\ (HIM)$	$C = 0.235,\ \alpha = 0.796$	$C = 0.501,\ \alpha = 0.529$	34%
$Figure\ 6\ (HIM)$	$C = 0.222,\ \alpha = 0.660$	$C = 0.568,\ \alpha = 0.416$	37%
$Figure\ 7\ (HIM)$	$C = 0.240,\ \alpha = 0.668$	$C = 0.534,\ \alpha = 0.409$	39%
$Figure\ 8\ (HIM)$	$C = 0.225,\ \alpha = 0.568$	$C = 0.484,\ \alpha = 0.440$	23%

4. Concluding Remarks

There are many types of image sharpening methods, with varying performance and usefulness in a given application. The method presented here was found to work exceptionally well in revealing fine details that are barely perceptible in SEM and HIM images. Future work will explore the use of contrast-limited adaptive histogram equalization, (CLAHE) in preconditioning the images, rather than AHE. The use of Lipschitz exponents will be a useful measurement tool in comparing these two procedures.

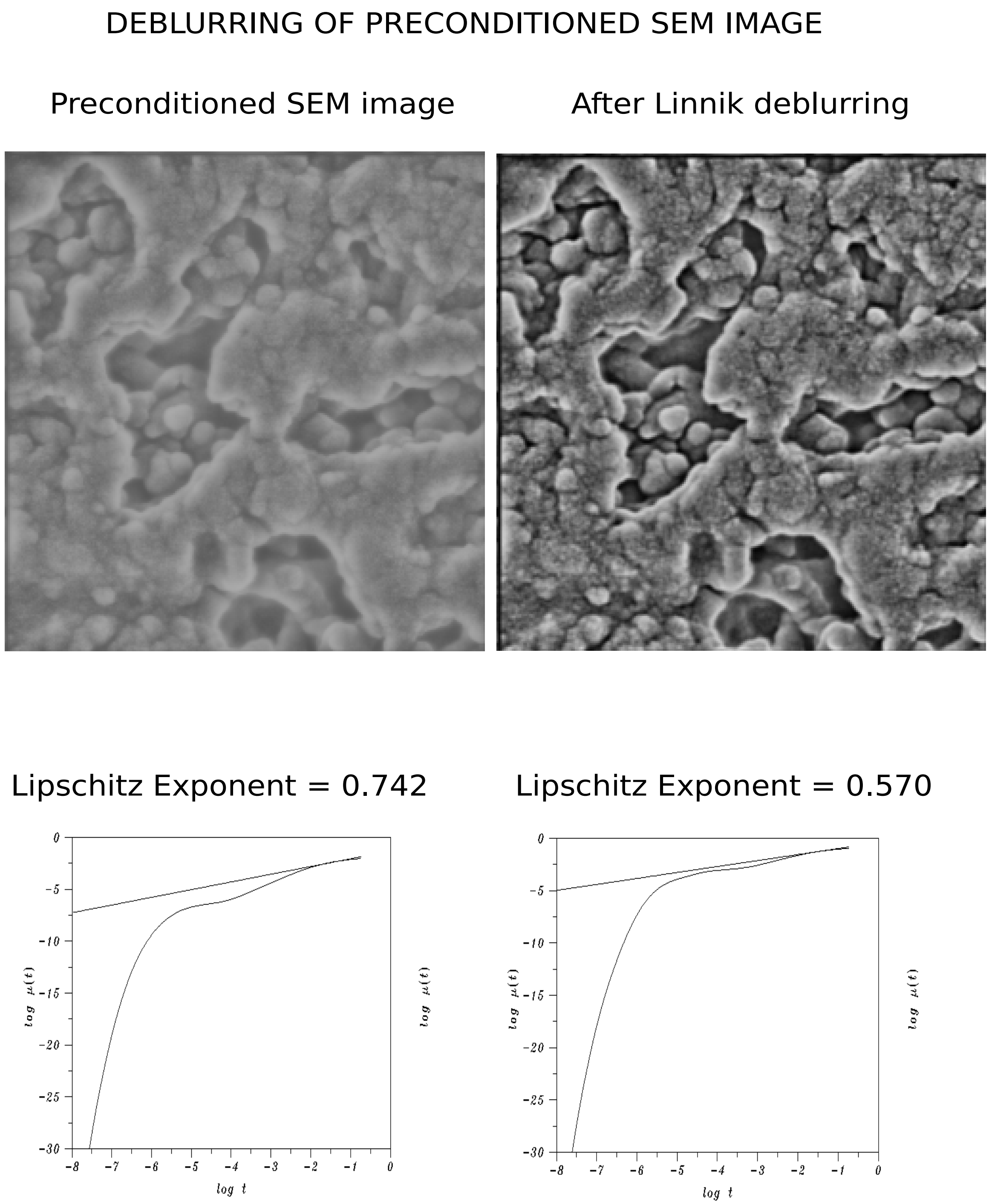

Secondary electron images of an etched glass sample.
In all $\log \mu(t)$ curved plots, $\mu(t) = \parallel U^t f - f \parallel_1 / \parallel f \parallel_1$, as in Eqs. (11). In lower left plot, straight line defined by $\log \mu(t) = -1.32 + 0.742 \log\ t$, majorizes $\log \mu(t)$ curve for $-2.0 < \log\ t < -1.0$, and implies $\parallel U^t f - f \parallel_1 \leq 0.267 \parallel f \parallel_1 t^{0.742},\ 0 < t \leq 0.1$. In lower right plot, straight line defined by $\log \mu(t) = -0.412 + 0.570 \log\ t$, majorizes $\log \mu(t)$ curve for $-2.0 < \log\ t < -1.0$, and implies $\parallel U^t f - f \parallel_1 \leq 0.662 \parallel f \parallel_1 t^{0.570},\ 0 < t \leq 0.1$.

Figure 1. $1\mu m$ HFW images.

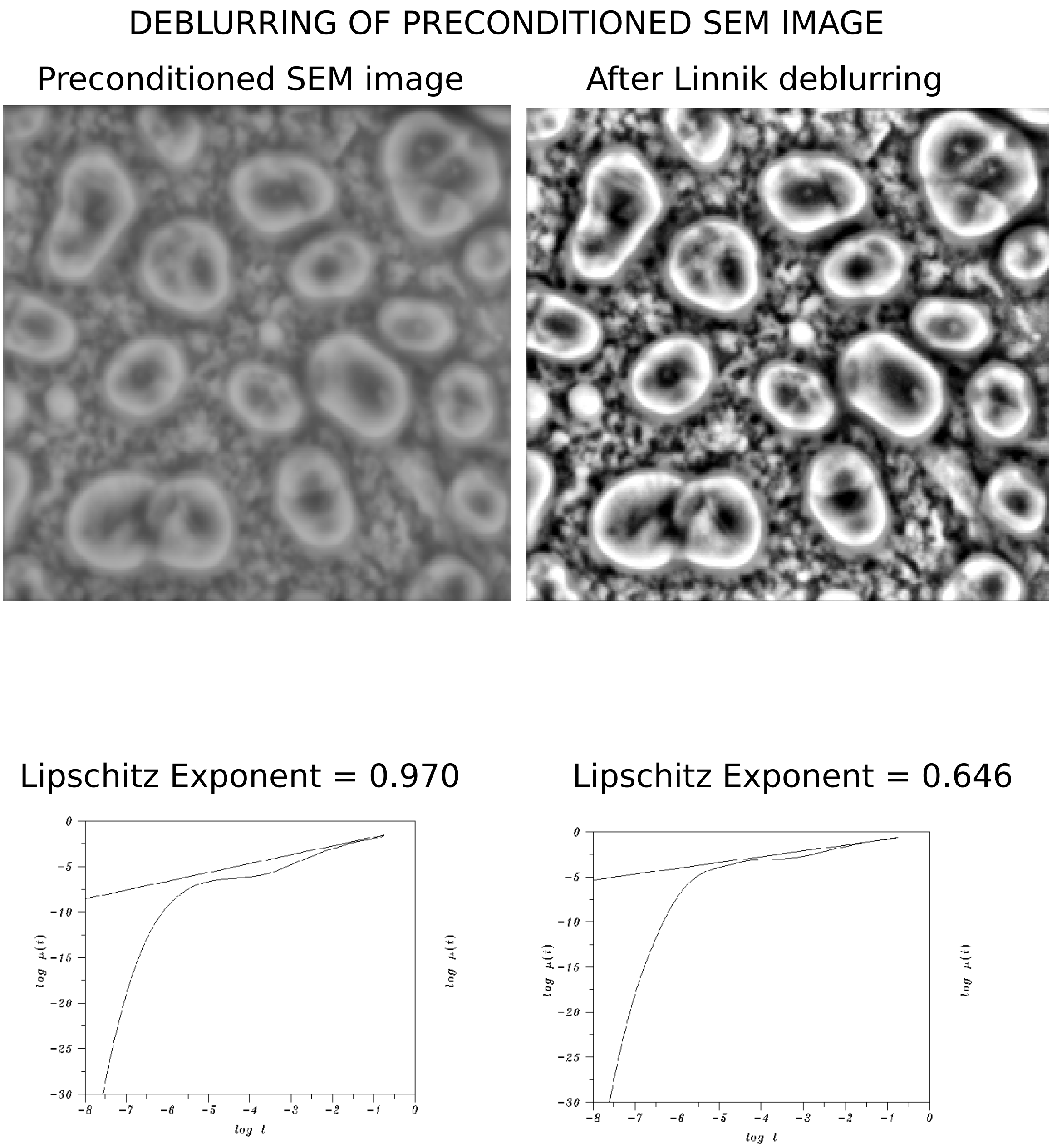

Au nanoparticles on Si substrate.
In all $\log \mu(t)$ curved plots, $\mu(t) = \| U^t f - f \|_1 \,/\, \| f \|_1$, as in Eqs. (11). In lower left plot, straight line defined by $\log \mu(t) = -0.792 + 0.970 \log\ t$, majorizes $\log \mu(t)$ curve for $-2.0 < \log\ t < -1.0$, and implies $\| U^t f - f \|_1 \leq 0.453 \| f \|_1\ t^{0.970},\ 0 < t \leq 0.1$. In lower right plot, straight line defined by $\log \mu(t) = -0.170 + 0.646 \log\ t$, majorizes $\log \mu(t)$ curve for $-2.0 < \log\ t < -1.0$, and implies $\| U^t f - f \|_1 \leq 0.844 \| f \|_1\ t^{0.646},\ 0 < t \leq 0.1$.

Figure 2. $0.25 \mu m$ HFW images.

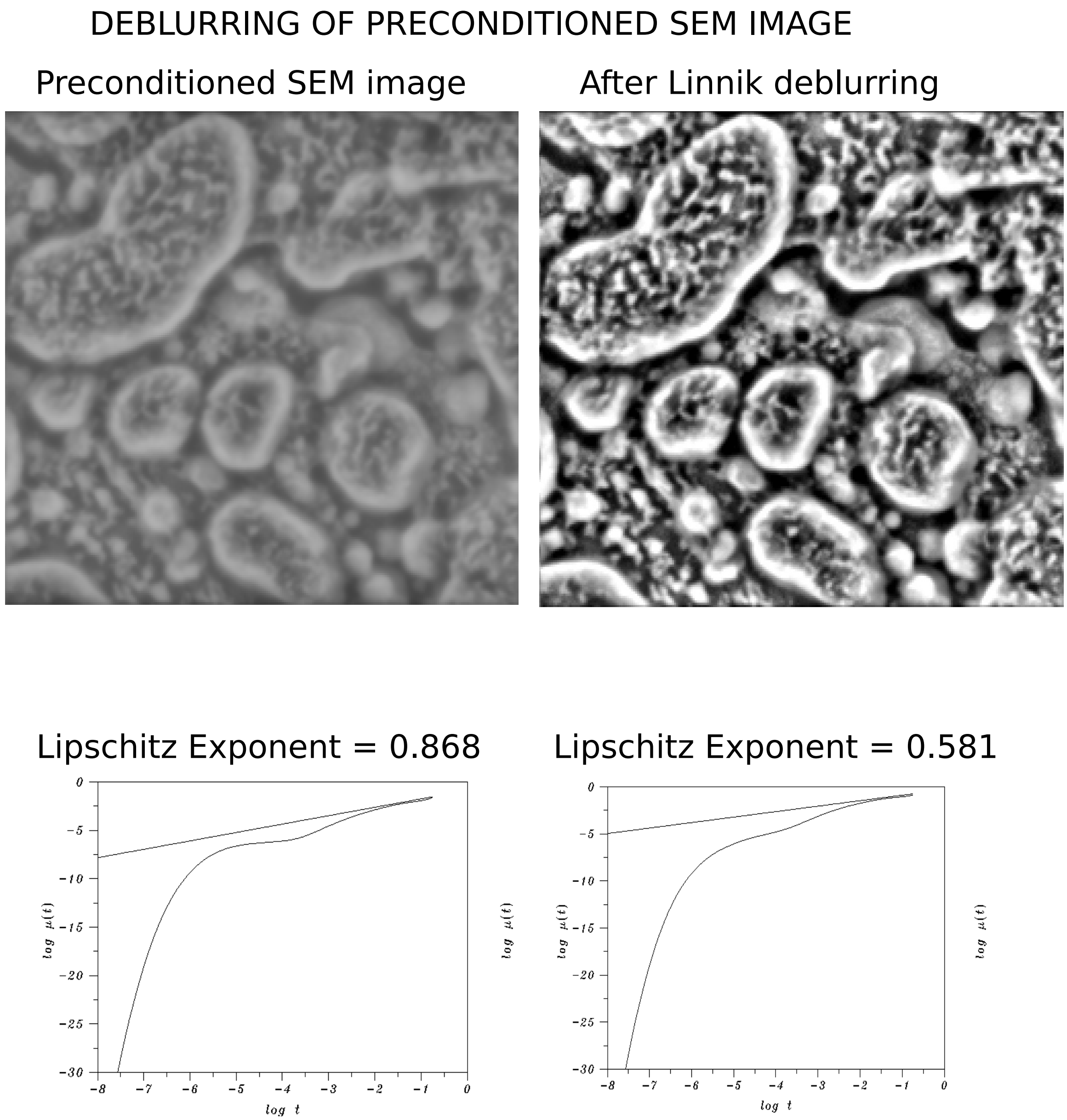

Au nanoparticles on C substrate.
In all $\log \mu(t)$ curved plots, $\mu(t) = \| U^t f - f \|_1 \,/\, \| f \|_1$, as in Eqs. (11). In lower left plot, straight line defined by $\log \mu(t) = -0.882 + 0.868 \log\ t$, majorizes $\log \mu(t)$ curve for $-2.0 < \log\ t < -1.0$, and implies $\| U^t f - f \|_1 \leq 0.414 \| f \|_1 \ t^{0.868},\ 0 < t \leq 0.1$. In lower right plot, straight line defined by $\log \mu(t) = -0.309 + 0.581 \log\ t$, majorizes $\log \mu(t)$ curve for $-2.0 < \log\ t < -1.0$, and implies $\| U^t f - f \|_1 \leq 0.734 \| f \|_1 \ t^{0.581},\ 0 < t \leq 0.1$.

Figure 3. $0.5 \mu m$ HFW images.

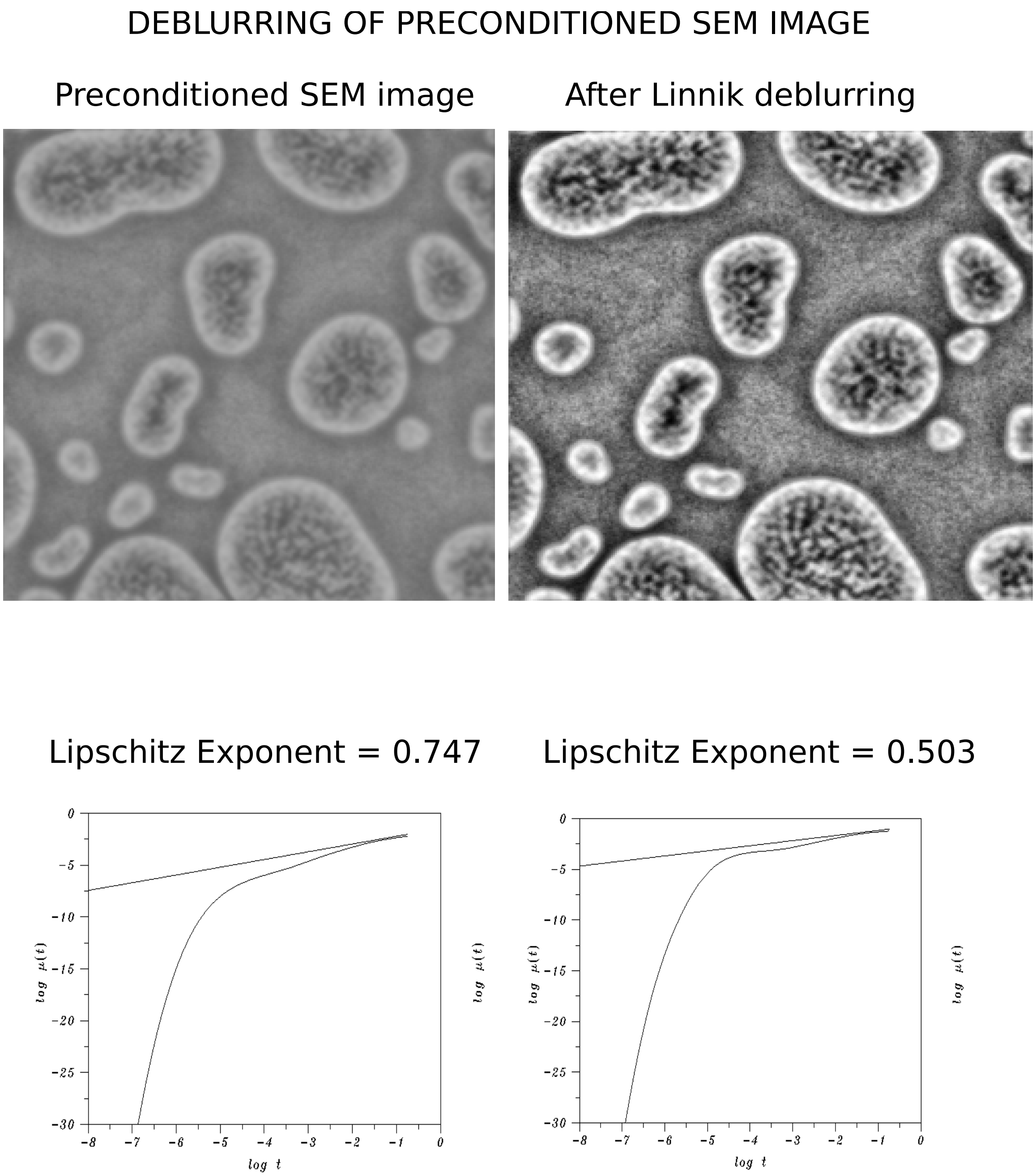

Au nanoparticles on Si substrate.
In all $\log \mu(t)$ curved plots, $\mu(t) = \parallel U^t f - f \parallel_1 / \parallel f \parallel_1$, as in Eqs. (11). In lower left plot, straight line defined by $\log \mu(t) = -1.474 + 0.747 \log\ t$, majorizes $\log \mu(t)$ curve for $-2.0 < \log\ t < -1.0$, and implies $\parallel U^t f - f \parallel_1 \leq 0.229 \parallel f \parallel_1\ t^{0.747},\ 0 < t \leq 0.1$. In lower right plot, straight line defined by $\log \mu(t) = -0.662 + 0.503 \log\ t$, majorizes $\log \mu(t)$ curve for $-2.0 < \log\ t < -1.0$, and implies $\parallel U^t f - f \parallel_1 \leq 0.516 \parallel f \parallel_1\ t^{0.503},\ 0 < t \leq 0.1$.

Figure 4. $0.50 \mu m$ HFW images.

DEBLURRING OF PRECONDITIONED HIM IMAGE

Preconditionned HIM image | After Linnik deblurring

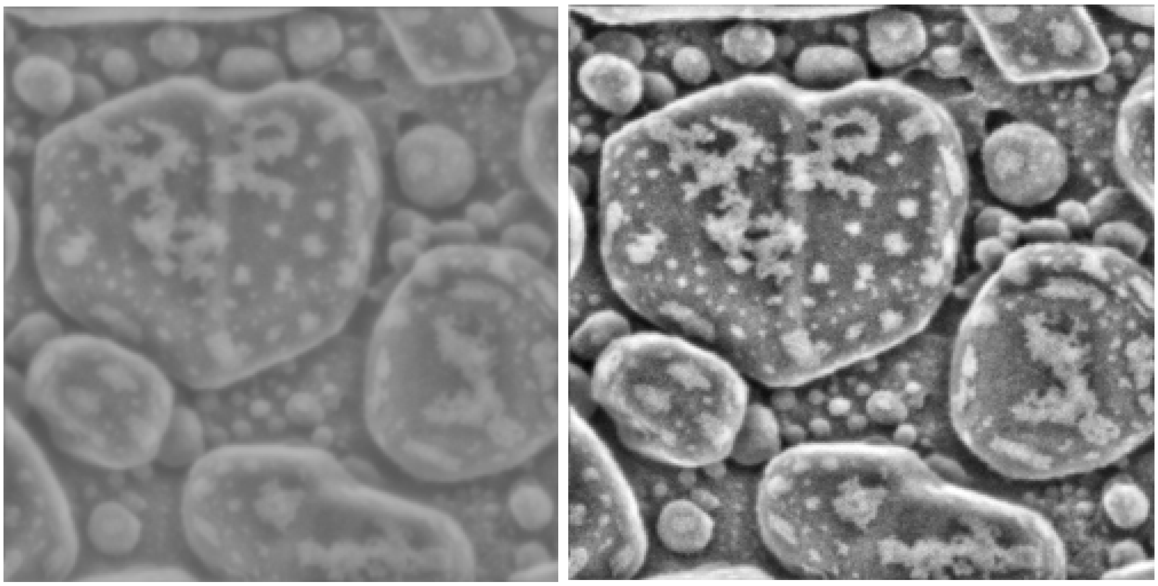

Lipschitz Exponent = 0.796 | Lipschitz Exponent = 0.529

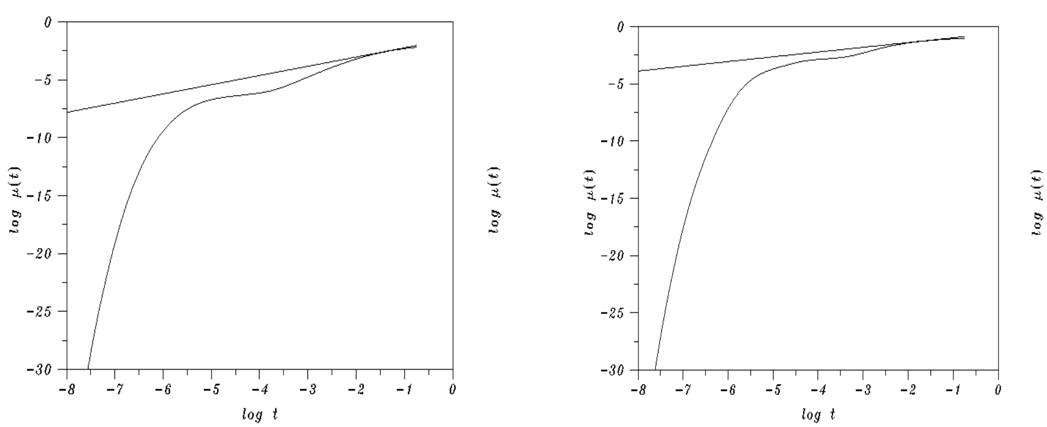

Pt-decorated Au nanoparticles on C substrate.

In all $\log \mu(t)$ curved plots, $\mu(t) = \| U^t f - f \|_1 \,/\, \| f \|_1$, as in Eqs. (11). In lower left plot, straight line defined by $\log \mu(t) = -1.448 + 0.796 \log\ t$, majorizes $\log \mu(t)$ curve for $-2.0 < \log\ t < -1.0$, and implies $\| U^t f - f \|_1 \leq 0.235 \,\| f \|_1\, t^{0.796},\ 0 < t \leq 0.1$. In lower right plot, straight line defined by $\log \mu(t) = -0.692 + 0.529 \log\ t$, majorizes $\log \mu(t)$ curve for $-2.0 < \log\ t < -1.0$, and implies $\| U^t f - f \|_1 \leq 0.501 \,\| f \|_1\, t^{0.529},\ 0 < t \leq 0.1$.

Figure 5. $0.50 \mu m$ HFW HIM images.

DEBLURRING OF PRECONDITIONED HIM IMAGE

Preconditioned HIM image | After Linnik deblurring

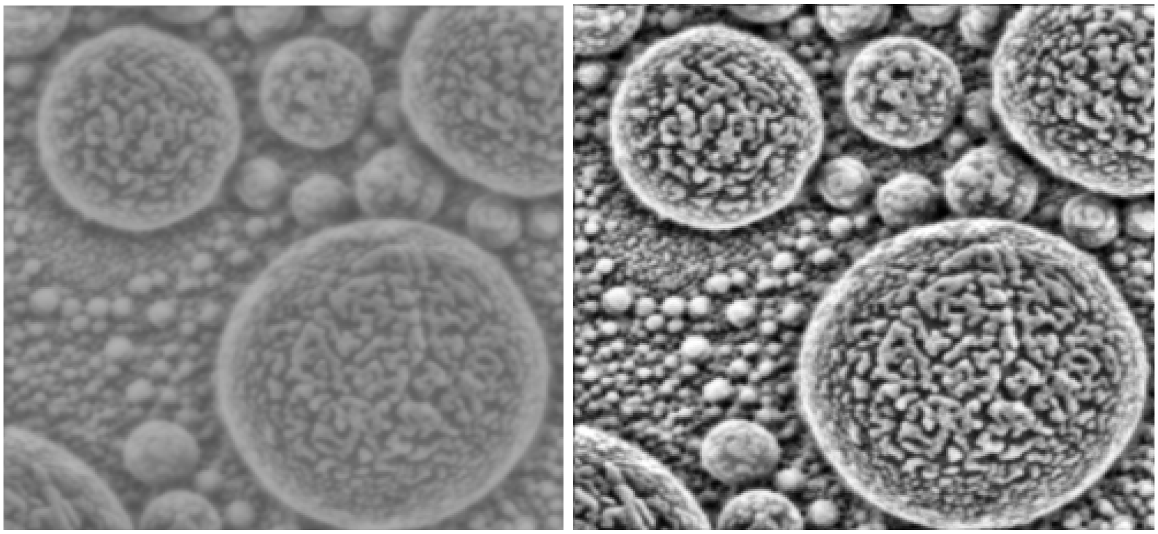

Lipschitz Exponent = 0.660 | Lipschitz Exponent = 0.416

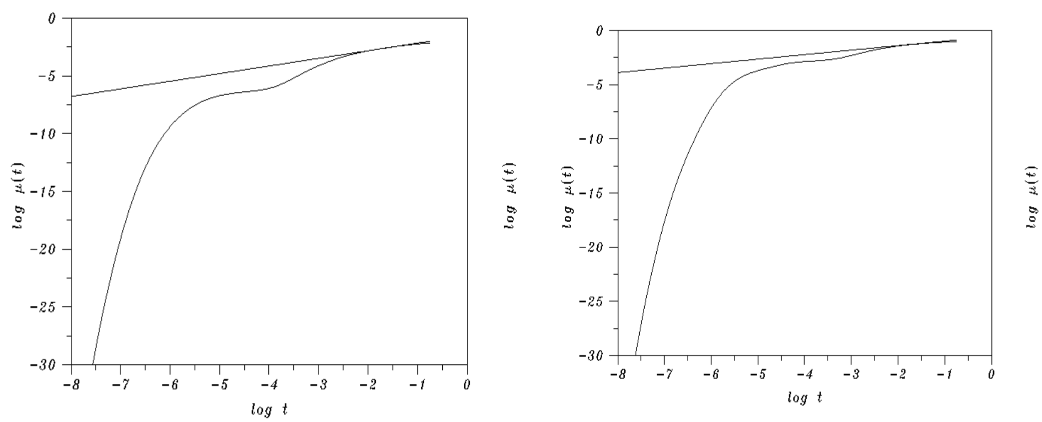

Pt-decorated tinballs on Si substrate.
In all $\log \mu(t)$ curved plots, $\mu(t) = \| U^t f - f \|_1 \;/\; \| f \|_1$, as in Eqs. (11). In lower left plot, straight line defined by $\log \mu(t) = -1.504 + 0.660 \log\ t$, majorizes $\log \mu(t)$ curve for $-2.0 < \log\ t < -1.0$, and implies $\| U^t f - f \|_1 \leq 0.222 \| f \|_1\ t^{0.660},\ 0 < t \leq 0.1$. In lower right plot, straight line defined by $\log \mu(t) = -0.566 + 0.416 \log\ t$, majorizes $\log \mu(t)$ curve for $-2.0 < \log\ t < -1.0$, and implies $\| U^t f - f \|_1 \leq 0.568 \| f \|_1\ t^{0.416},\ 0 < t \leq 0.1$.

Figure 6. $5.0\mu m$ HFW HIM images.

DEBLURRING OF PRECONDITIONED HIM IMAGE

Preconditioned HIM image | After Linnik deblurring

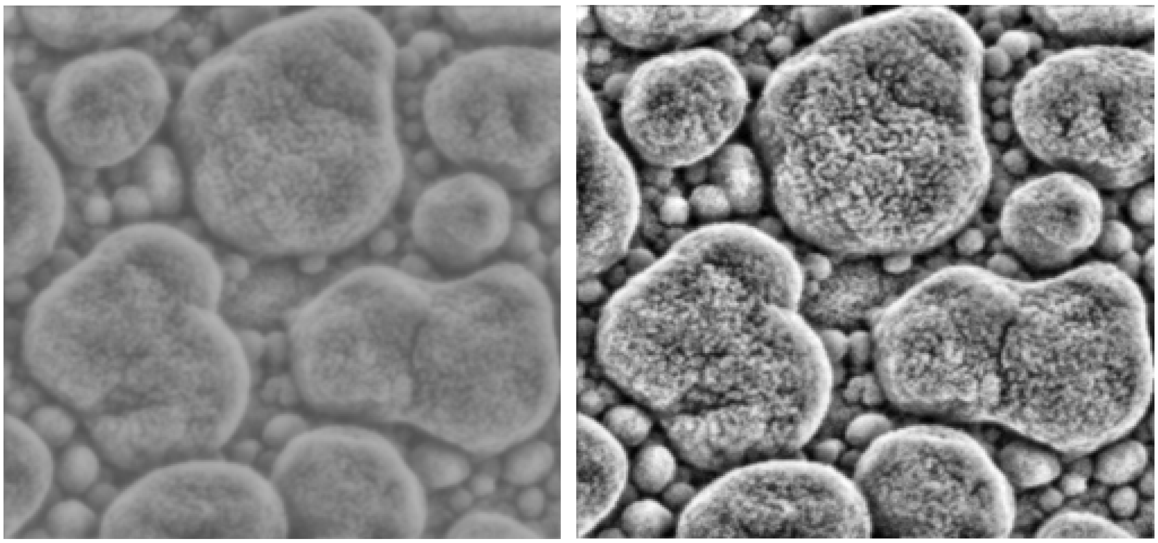

Lipschitz Exponent = 0.688 | Lipschitz Exponent = 0.409

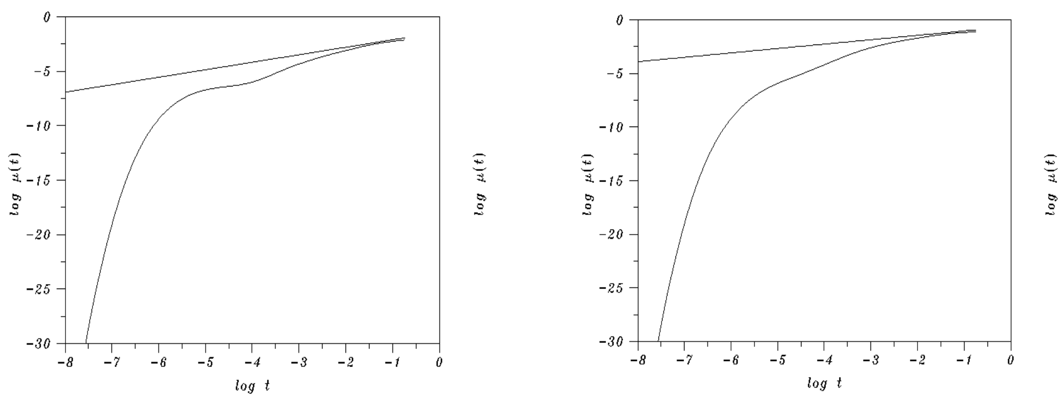

Au nanoparticles on C substrate.
In all $\log \mu(t)$ curved plots, $\mu(t) = \| U^t f - f \|_1 \, / \, \| f \|_1$, as in Eqs. (11). In lower left plot, straight line defined by $\log \mu(t) = -1.426 + 0.688 \log \ t$, majorizes $\log \mu(t)$ curve for $-2.0 < \log \ t < -1.0$, and implies $\| U^t f - f \|_1 \leq 0.240 \| f \|_1 \ t^{0.688}, \ 0 < t \leq 0.1$. In lower right plot, straight line defined by $\log \mu(t) = -0.628 + 0.409 \log \ t$, majorizes $\log \mu(t)$ curve for $-2.0 < \log \ t < -1.0$, and implies $\| U^t f - f \|_1 \leq 0.534 \| f \|_1 \ t^{0.409}, \ 0 < t \leq 0.1$.

Figure 7. $2.0 \mu m$ HFW HIM images.

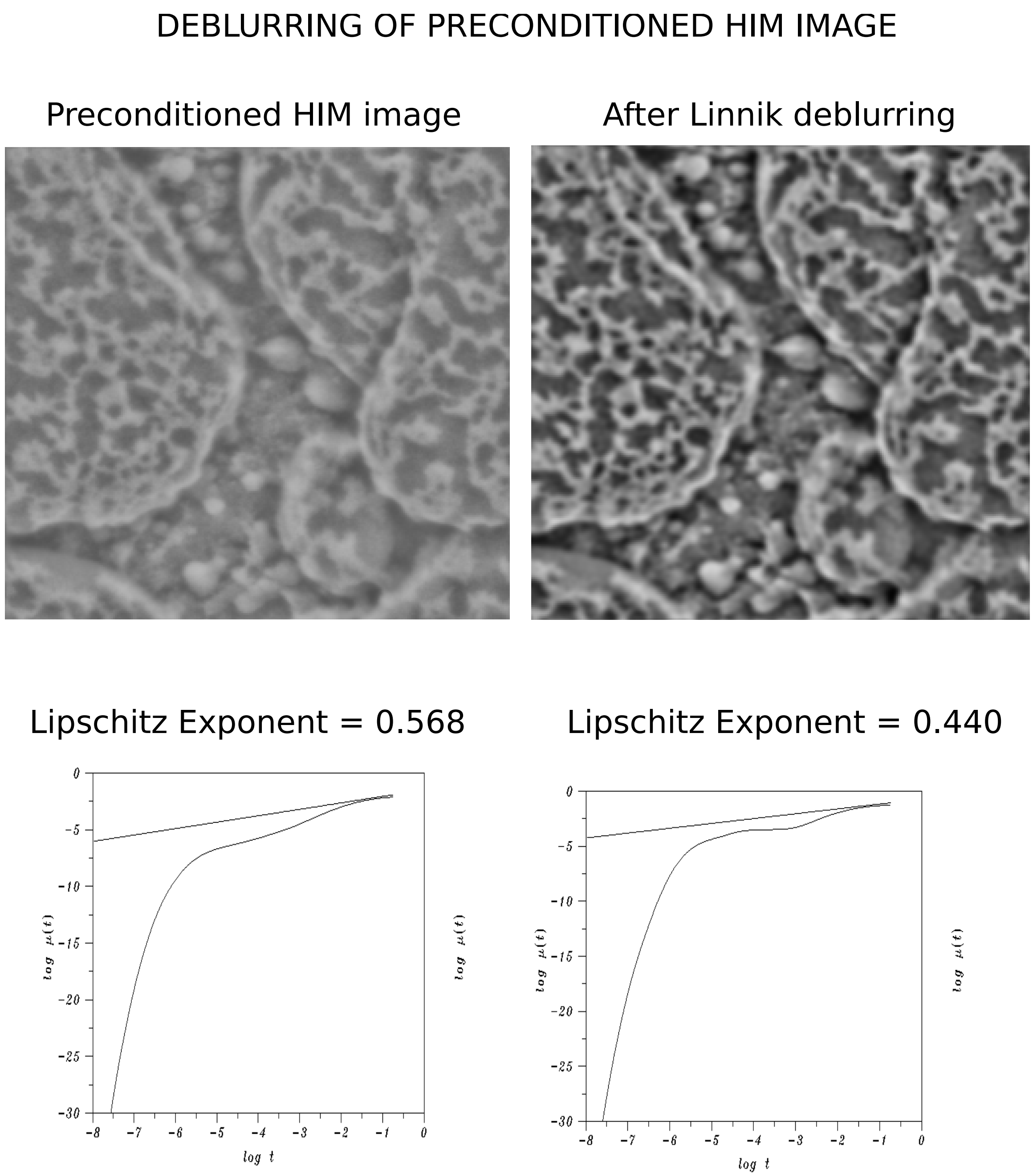

Pt-decorated Au nanoparticles on C substrate.
In all $\log \mu(t)$ curved plots, $\mu(t) = \| U^t f - f \|_1 \ / \ \| f \|_1$, as in Eqs. (11). In lower left plot, straight line defined by $\log \mu(t) = -1.491 + 0.568 \log \ t$, majorizes $\log \mu(t)$ curve for $-2.0 < \log \ t < -1.0$, and implies $\| U^t f - f \|_1 \leq 0.225 \ \| f \|_1 \ t^{0.568}, \ 0 < t \leq 0.1$. In lower right plot, straight line defined by $\log \mu(t) = -0.725 + 0.440 \log \ t$, majorizes $\log \mu(t)$ curve for $-2.0 < \log \ t < -1.0$, and implies $\| U^t f - f \|_1 \leq 0.484 \ \| f \|_1 \ t^{0.440}, \ 0 < t \leq 0.1$.

Figure 8. $0.5\mu m$ HFW HIM images.

References

[1] A. S. Carasso and A. E. Vladár (2024) Linnik point spread functions, time-reversed logarithmic diffusion equations, and blind deconvolution of electron microscope imagery. (National Institute of Standards and Technology, Gaithersburg, MD), NIST Technical Note (TN), NIST TN 2324. https://doi.org/10.6028/NIST.TN.2324

[2] A. S. Carasso (2004) Singular integrals, image smoothness, and the recovery of texture in image deblurring. *SIAM J Appl Math* 64:1749–1774. https://doi.org/10.1137/S0036139903428306

[3] A. S. Carasso and A. E. Vladár (2008) Calibrating image roughness by estimating Lipschitz exponents, with application to image restoration. *Optical Engineering* 47(037012):45–47. https://doi.org/10.1117/1.2899144

[4] A. S. Carasso (2010) Bochner subordination, logarithmic diffusion equations, and blind deconvolution of Hubble space telescope imagery and other scientific data. *SIAM Journal on Imaging Sciences* 3:954–980. https://doi.org/10.1137/090780225

[5] A. S. Carasso and A. E. Vladár (2012) Fractional diffusion, low exponent Lévy stable laws, and 'slow motion' denoising of helium ion microscope nanoscale imagery. *Journal of Research of the National Institute of Standards and Technology* 117:119–142. https://doi.org/10.6028/jres.117.006

[6] M. H. Taibleson (1964) On the theory of Lipschitz spaces of distributions on Euclidean n-space: I. Principal properties. *J Math Mechanics* 13:407–478.